ADVANCED ENERGY MATERIALS
www.advenergymat.de

Ultrahigh-Pressure Structural Modification in BiCuSeO Ceramics: Dense Dislocations and Exceptional Thermoelectric Performance

Zhanxiang Yin, He Zhang, Yaqiang Wang, Yi Wu, Youbo Xing, Xue Wang, Xufei Fang, Yuan Yu,* and Xin Guo**

Dislocations as line defects in crystalline solids play a crucial role in controlling the mechanical and functional properties of materials. Yet, for functional ceramic oxides, it is very difficult to introduce dense dislocations because of the strong chemical bonds. In this work, the introduction of high-density dislocations is demonstrated by ultrahigh-pressure sintering into a typical ceramic oxide, BiCuSeO, for thermoelectric applications. The ultrahigh-pressure induces shear stresses that surpass the critical strength for dislocation nucleation, followed by dislocation glide and profuse multiplication, leading to a high dislocation density of ≈9.1 × 10^{16} m^{-2} in $Bi_{0.96}Pb_{0.04}CuSeO$ ceramic. These dislocations greatly suppress the phonon transport to reduce the lattice thermal conductivity, reaching 0.13 Wm^{-1} K^{-1} at 767 K and resulting in a record-high zT of 1.69 in this oxide thermoelectric ceramic. This study demonstrates the feasibility of generating dense dislocations in ceramic oxides via ultrahigh-pressure sintering for tuning functional properties.

1. Introduction

Dislocations are linear crystallographic imperfections that distort the arrangement of atoms in a periodic lattice.[1] The plastic deformation of metals is mediated primarily by the multiplication and movement of dislocations. In this regard, the density and spatial arrangement of dislocations influence the mechanical properties of metals.[2] In semiconductors with covalent/ionic bonds, dislocations can be charged due to the formation of dangling bonds and charge transfer.[3,4] This electrostatic effect builds a potential barrier to scatter and trap charge carriers, reducing carrier mobility in semiconductors.[5,6] Thus, dislocations are undesirable for most of the semiconductor applications. However, dislocations have also been shown effective in scattering heat-carrying phonons and thus lower the thermal conductivity.[7,8] This phenomenon is highly desirable for the property enhancement of thermoelectric materials.[8,9] The thermal-to-electricity energy conversion efficiency of a material is determined by the thermoelectric figure-of-merit, $zT = S^2\sigma T/(\kappa_e+\kappa_l)$. Here, S is the Seebeck coefficient, σ is the electrical conductivity, T is the absolute temperature, κ_e is the electronic thermal conductivity, and κ_l is the lattice thermal conductivity. It is apparent that the lower the κ_l, the higher the zT value.

Introducing dislocations to reduce κ_l and thus improve zT has been realized in many typical thermoelectric materials.[9,10] For example, dislocations-induced low κ_l approaching the theoretical minimum has been achieved in $Bi_{0.5}Sb_{1.5}Te_3$,[11] PbSe,[12] PbTe,[13] and SnTe[14] alloys by various processing methods such

Z. Yin, H. Zhang, Y. Wang, Y. Wu, Y. Xing, X. Guo
School of Materials Science and Engineering
Changchun University of Science and Technology
Changchun 130022, China
E-mail: xguo@cust.edu.cn

X. Wang
School of Science
ShanDong JiaoTong University
Jinan 250357, China

X. Fang
Institute for Applied Materials
Karlsruhe Institute of Technology
Kaiserstrasse 12, 76131 Karlsruhe, Germany
E-mail: xufei.fang@kit.edu

Y. Yu
Institute of Physics (IA)
RWTH Aachen University
52056 Aachen, Germany
E-mail: yu@physik.rwth-aachen.de

X. Guo
Engineering Research Center of Optoelectronic Functional Materials
Ministry of Education
Changchun 130022, China

The ORCID identification number(s) for the author(s) of this article can be found under https://doi.org/10.1002/aenm.202403174

DOI: 10.1002/aenm.202403174

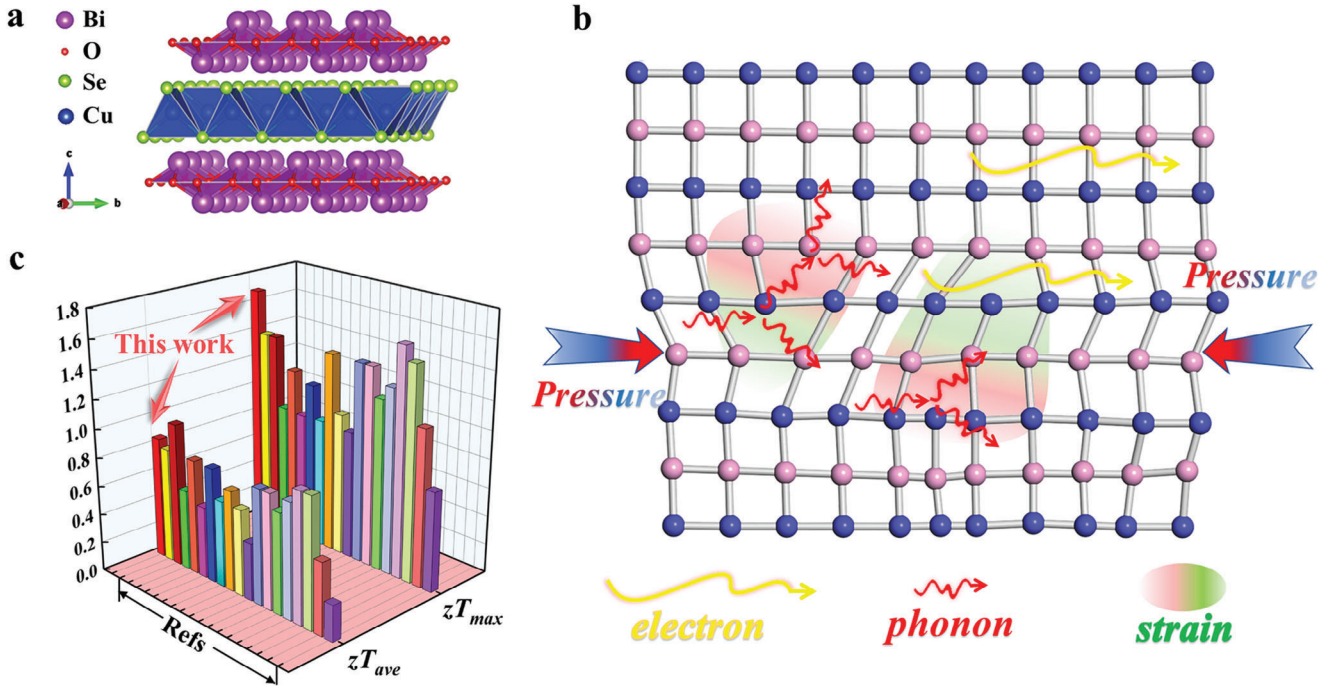

Figure 1. Schematics for crystal structure, phonon transport, and thermoelectric performance. a) Crystal structure of BiCuSeO. b) Scattering mechanisms of phonons. c) Comparison of thermoelectric performances of optimum BiCuSeO and this work.[18–21,23–36]

as liquid-phase sintering, interstitial doping, and annealing vacancies. However, compared to metals and these metavalently bonded chalcogenides,[15] it remains a colossal challenge to introduce high-density dislocations in ceramic oxides through conventional methods because of the strong covalent/ionic bonds,[16] rendering little plasticity in most ceramic oxides. This also largely retards the manipulation of functional properties, e.g., the thermoelectric performance of many ceramic oxides upon dislocation engineering.

With the emergence of ultrahigh-pressure (UHP) sintering techniques (the order of gigapascal pressure, ≈GPa), the nucleation and multiplication of dislocations in ceramics become readily feasible. For instance, it has been experimentally established that dislocation nucleation in ceramics requires shear stress beyond GPa to break the bonds to form dislocations.[17] Thus, the ultrahigh-pressure sintering technique provides an opportunity to enable dislocation-tuned functional properties of ceramics. Among a plethora of ceramics, BiCuSeO has been attracting ever-increasing attention for thermoelectric applications due to many advantages including earth-abundant constituting elements, high stability, environmental friendly, and decent thermoelectric performance.[18–21] With high dislocation densities being introduced into BiCuSeO to further lower its κ_l, it can be a promising approach to greatly enhance its thermoelectric properties for much broader applications.

In this work, we have achieved high-density dislocations of ≈9.1×10^{16} m^{-2} in BiCuSeO ceramics prepared under 2 GPa using the UHP sintering method. We investigated the mechanisms underpinning dislocation nucleation and multiplication under gigapascal pressure, based on structural characterizations using transmission electron microscopy (TEM) and atom probe tomography (APT). Owing to dense dislocations enabled by ultrahigh pressure, a low κ_l of 0.13 Wm^{-1} K^{-1} was achieved at 767 K and approaches the diffusive thermal conductivity limit (κ_{diff} ≈0.07 Wm^{-1} K^{-1}) of BiCuSeO.[22] This also directly results in a record-high zT value of 1.69 at 767 K for BiCuSeO-based compounds reported so far,[18–21,23–36] as illustrated in **Figure 1**. Most importantly, our work demonstrates the feasibility of introducing high-density dislocations in ceramic oxides through ultrahigh-pressure techniques. We also provide insights into the mechanism of pressure-induced dislocations and the resulting impact on tuning the functional properties beyond thermoelectricity.

2. Results and Discussion

2.1. Superior $Bi_{1-x}Pb_xCuSeO$ Ceramics Selected Based on Ultrahigh-Pressure Process

Optimizing the carrier concentration is often the foremost step in tuning the electrical transport properties of thermoelectric materials.[20,37] The pristine p-type BiCuSeO shows an intrinsically low carrier concentration of ≈10^{18} cm^{-3} and thus a low electrical conductivity.[38] Pb has been proven one of the most efficient dopants to tune the carrier concentration of BiCuSeO.[18,20,32] Herein, we also utilize Pb to substitute for the position of Bi in conjunction with the UHP technique introduced during the sample preparation process to optimize the power factor. To initially evaluate the evolution of room-temperature thermoelectric performance driven by pressure, $Bi_{1-x}Pb_xCuSeO$ ceramics (with x = 0, 0.02, 0.04, 0.06, and 0.08) were prepared under 1–3.5 GPa with a step size of 0.5 GPa (details in Experimental Section, and Figure S1, Supporting Information). The electrical

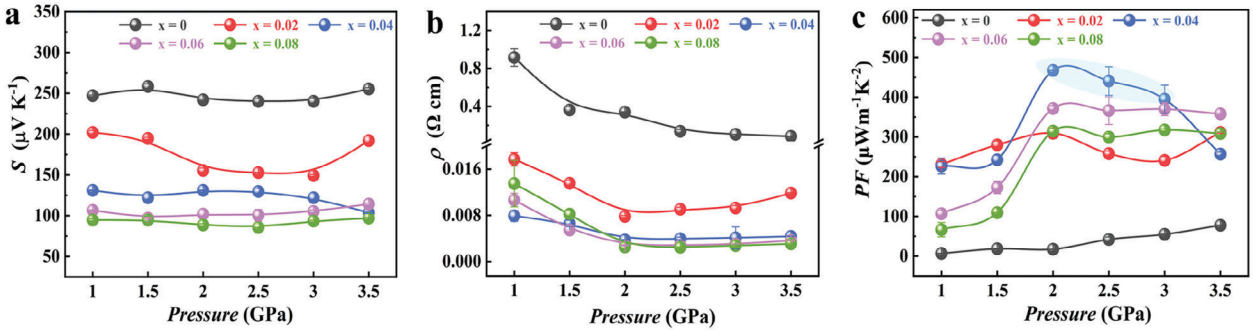

Figure 2. Optimization of pressure and composition for $Bi_{1-x}Pb_xCuSeO$ ceramics. Room-temperature a) Seebeck coefficient, *S*, b) electrical resistivity, ρ, and c) power factor, *PF*.

transport properties as a function of both the sintering pressure and the content of Pb are shown in **Figure 2**. The Seebeck coefficient and electrical resistivity in general decrease with increasing Pb content regardless of the sintering pressure due to the increased charge carrier concentration by introducing Pb at the Bi sites. Note that the small difference in properties at a Pb content higher than 4% could be due to the supersaturation of the Pb doping effect in the matrix. Besides the chemical composition, the electrical properties also change significantly with the sintering pressure. Figure 2a illustrates that the Seebeck coefficient is not very sensitive to the sintering pressure for all samples studied. In contrast, the electrical resistivity first decreases and then slightly increases with increasing pressure, reaching a minimum of 2 GPa for all Pb-doped samples. It has been demonstrated in many thermoelectrics such as Bi_2Te_3,[39] ZnO,[40] and PbTe,[41] that the solubility of dopants in the matrix increases due to the introduction of high pressure. Owing to the solubility behavior associated with pressure, the content of Pb in the BiCuSeO matrix may reach the solubility limit at ≈4% when the pressure is 1 GPa. A Pb content higher than 4% would thus increase the resistivity because of the supersaturation, as observed in Figure 2b. Based on the improved solubility of Pb in the BiCuSeO matrix upon increasing the pressure, the resistivity of the heavily doped samples, i.e., with 6% and 8% Pb, decreases with increasing pressure until 2 GPa. Yet, further increasing the pressure to 3.5 GPa can only slightly improve the solubility of Pb, leading to comparable electrical resistivity among samples with a higher Pb content above 2 GPa. As a result of chemical composition optimization and UHP sintering, large power factors are obtained in $Bi_{0.96}Pb_{0.04}CuSeO$ ceramics sintered under 2, 2.5, and 3 GPa. We will then focus on the temperature-dependent thermoelectric performance of $Bi_{0.96}Pb_{0.04}CuSeO$ ceramics prepared under the optimum pressure ranges of 2, 2.5, and 3 GPa. In addition, to adequately reveal the influence of ultrahigh-pressure on the transport properties, a control sample ($Bi_{0.96}Pb_{0.04}CuSeO$) is also prepared by a conventional approach (CA) sintered under the pressure of 50 MPa (hot-press sintering, Figure S1, Supporting Information) for comparison with the UHP ones.

2.2. Lattice Thermal Conductivity and Dislocation Density

The temperature-dependent σ, *S*, and κ of $Bi_{0.96}Pb_{0.04}CuSeO$ ceramics are displayed in Figure S2 (Supporting Information). The electrical conductivity (Figure S2a, Supporting Information) is slightly decreased for the UHP samples compared with the CA sample. Interestingly, a similar trend is also observed for the Seebeck coefficient (Figure S2b, Supporting Information). This contradicts the normal relationship between the electrical conductivity and the Seebeck coefficient depending on the carrier concentration. Actually, the carrier concentration decreases with increasing the sintering pressure (Figure S2c, Supporting Information), which should increase the Seebeck coefficient. The Pisarenko plot shows that the reduced Seebeck coefficient is mainly ascribed to the decreased density-of-states effective mass (m^*). The CA sample exhibits a m^* value of 3.9 m_e, where m_e is the electron mass, which is comparable to other BiCuSeO-based ceramics prepared under normal pressure.[28,29,34] In contrast, the m^* value decreases to only 1.1 m_e under a pressure of 3 GPa. It has been theoretically and experimentally demonstrated that the UHP increases the bandgaps and elevates the light-hole bands toward the Fermi level in BiCuSeO,[42–44] leading to the reduction of carrier concentration and m^* responsible for the variations in the electrical conductivity and Seebeck coefficient. Figure 2d shows that the total thermal conductivity (κ) of $Bi_{0.96}Pb_{0.04}CuSeO$ prepared under ultrahigh pressure is much lower than that of the control sample (CA), but little variation in κ for the samples prepared above 2 GPa (Figure S3, Supporting Information). This could mean a critical pressure that exists in achieving low thermal conductivity, which will be elaborated on in the following text. In contrast to the largely lowered thermal conductivity for the UHP-prepared samples, the electrical conductivity only slightly deteriorates under the UHP sintering. This indicates a strong reduction in the lattice thermal conductivity. The temperature-dependent κ_l is calculated by subtracting κ_e from κ (**Figure 3a**). The κ_e can be determined using the Wiedemann–Franz law, $\kappa_e = L\sigma T$, where *L* is the Lorenz number estimated by fitting the Seebeck coefficient to the reduced chemical potential (details in Supporting Information, Figure S4, Supporting Information). Figure 3a indicates that the κ_l is significantly suppressed with a dramatic drop from 0.7 Wm^{-1} K^{-1} for the control sample to 0.25 Wm^{-1} K^{-1} for the UHP sintered samples at 374 K. This big gap for κ_l between the control and other samples remains throughout the entire measurement temperature range. This implies that the heat-carrying phonons are heavily scattered in $Bi_{0.96}Pb_{0.04}CuSeO$ ceramics prepared under ultrahigh pressure. To understand the mechanisms responsible for the difference in thermal transport properties between the control and UHP-prepared samples from a perspective

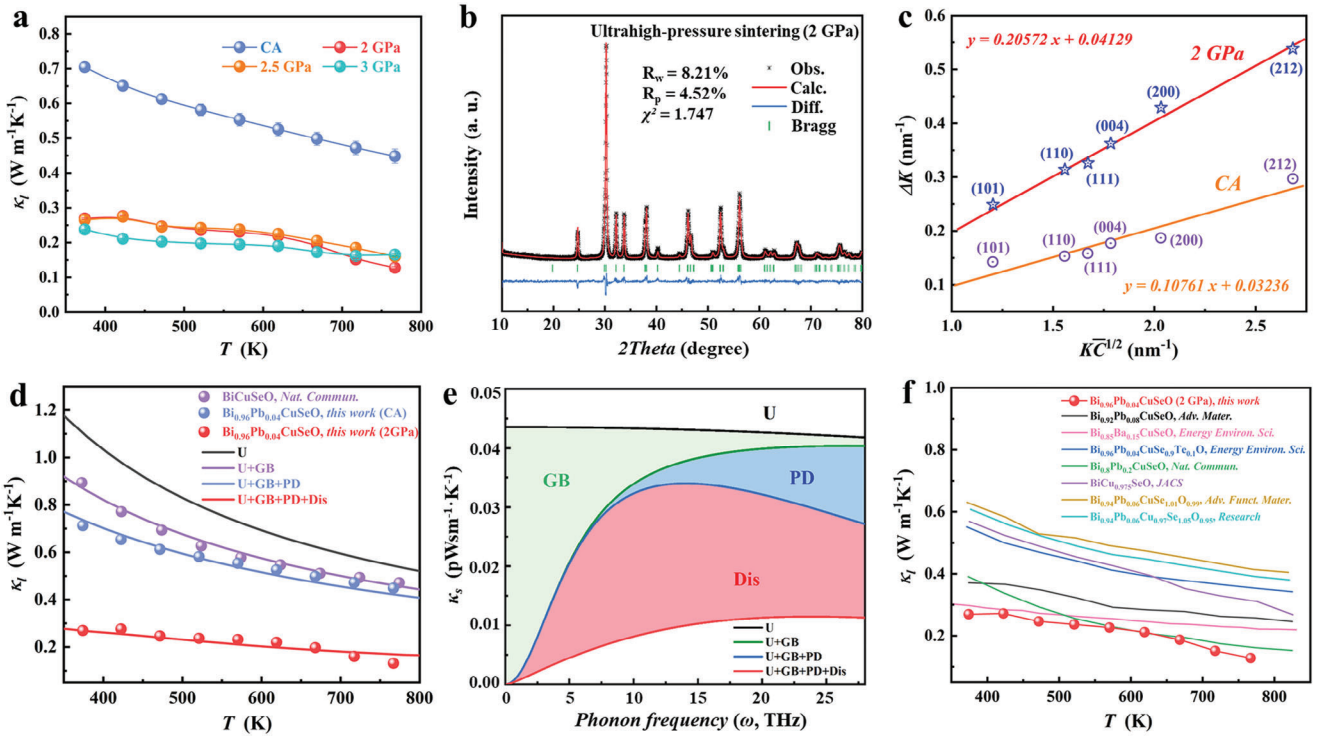

Figure 3. Lattice thermal conductivity and ΔK–$K\bar{C}^{1/2}$ Plots obtained by the mWH method. a) Lattice thermal conductivity of $Bi_{0.96}Pb_{0.04}CuSeO$ ceramics prepared under different conditions. b) Rietveld refinement analysis for XRD data of $Bi_{0.96}Pb_{0.04}CuSeO$ ceramics prepared under 2 GPa. c) ΔK versus $K\bar{C}^{1/2}$ relationship of CA (control sample) and UHP $Bi_{0.96}Pb_{0.04}CuSeO$ ceramics. d) Experimental κ_l compared with predicted κ_l determined by the Debye–Callaway model. e) Calculated κ_s with different scattering mechanisms in $Bi_{0.96}Pb_{0.04}CuSeO$ ceramics prepared under 2 GPa. f) Comparison of the κ_l for BiCuSeO-based ceramics.[18–21,24,47,50]

of microstructures, we first analyzed the X-ray diffraction (XRD) data for the samples prepared by conventional approach and under 2 GPa via the Rietveld refinement method (Figure 3b; Figure S5, Supporting Information). The diffraction patterns for both samples can be indexed to the phase-pure $Bi_{0.96}Pb_{0.04}CuSeO$ ceramics. Furthermore, the XRD diffraction peak profiles are fitted by the Gaussian function to obtain the exact Bragg position and the full width at half maximum (FWHM), as listed in Table S1 (Supporting Information). Based on the XRD diffraction peak broadening effect, together with corresponding indices of crystal plane and FWHM (Table S1, Supporting Information), we find different values of dislocation density in these samples, as estimated by the modified Williamson-Hall (mWH) method (details in Supporting Information):[45,46]

$$\Delta K = \left(\pi A^2 b^2/2\right)^{1/2} N_D^{\frac{1}{2}} \left(K\bar{C}^{\frac{1}{2}}\right) + 0.9/d \quad (1)$$

in which $K = 2sin\theta/\lambda$ and $\Delta K = 2cos\theta(\Delta\theta)/\lambda$, where θ and λ are the diffraction angle and the wavelength of X-rays, d is the average grain size, b is the magnitude of Burgers vector, and N_D is the dislocation density. The relevant parameters used for the mWH method can be found in Tables S1–S3 (Supporting Information). Based on the mWH method, the ΔK–$K\bar{C}^{1/2}$ profiles are obtained in Figure 3c, which manifest a single linearity well corresponding to the asymptotic line-profile theory. Therefore, the dislocation density is calculated by the slope of the ΔK–$K\bar{C}^{1/2}$ plots. Eventually, the N_D of $Bi_{0.96}Pb_{0.04}CuSeO$ ceramics prepared under 2 GPa reaches $\approx 9.1 \times 10^{16}$ m^{-2}, which is much higher than $\approx 5.8 \times 10^{13}$ m^{-2} in the control (CA) sample and 3.0×10^{14} m^{-2} in the self-substituted BiCuSeO by Se at the O site reported recently.[47] Figure S6 (Supporting Information) shows the evolution of the N_D associated with UHP in the $Bi_{0.96}Pb_{0.04}CuSeO$ ceramics. Notably, the N_D greatly increases until 2 GPa while holding little variation for further increasing UHP, which implies that there is a critical pressure for introducing the N_D of the $Bi_{0.96}Pb_{0.04}CuSeO$ ceramics, and accounts for the similar κ values for the samples prepared above 2 GPa. All the dislocation densities of the UHP-prepared samples demonstrate a high order of magnitude ($\approx 10^{16}$ m^{-2}). Such a high dislocation density is very rare even in other ceramic materials.

These different dislocation densities can phenomenologically explain the κ_l by invoking the Debye–Callaway model (Figure 3d; Supporting Information), as expressed in Equation (2) below:[48]

$$\kappa_l = \frac{k_B}{2\pi^2 \upsilon}\left(\frac{k_B T}{\hbar}\right)^3 \int_0^{\frac{\theta_D}{T}} \tau_{tot}(x) \frac{x^4 e^x}{(e^x-1)^2} dx \quad (2)$$

where $x = \hbar\omega/k_B T$, k_B is the Boltzmann constant, ω is the angular frequency of phonon, υ is the average sound velocity, $\hbar$ is the reduced Planck constant, θ_D is the Debye temperature, and τ_{tot} is the total relaxation time. Given various scattering

mechanisms, the τ_{tot} can be determined by Matthiessen's rule (Equation (3)).[24,49]

$$\tau_{tot}^{-1} = \tau_U^{-1} + \tau_{GB}^{-1} + \tau_{PD}^{-1} + \tau_{Dis}^{-1} \quad (3)$$

where τ_U, τ_{GB}, τ_{PD}, and τ_{Dis} denote the phonon relaxation time of the Umklapp process, scattered by grain boundaries, point defects, and dislocations, respectively. Figure 3d shows the contribution of various scattering mechanisms to reducing κ_l. The Umklapp process leads to a relatively higher κ_l due to the absence of extra scattering events. By introducing grain boundaries for phonon scattering, the calculated value can fit well to a pristine polycrystalline BiCuSeO without the effects of doping and ultrahigh pressure.[20,37] The κ_l of the control $Bi_{0.96}Pb_{0.04}CuSeO$ sample further decreases compared with the Pb-free BiCuSeO. This can be explained by incorporating point defect phonon scattering due to the substitution of Bi by Pb, as indicated by the well-fitted κ_l curve in Figure 3d. Yet, these typical scattering sources observed in BiCuSeO are insufficient to account for the ultralow lattice thermal conductivity of the $Bi_{0.96}Pb_{0.04}CuSeO$ sample prepared under 2 GPa. The theoretical κ_l calculated by the Debye–Callaway model can only fit the experimental data by incorporating the dislocation phonon scattering using the N_D derived above. This reveals the origin of the substantially reduced κ_l in the UHP samples and verifies the reliability of the high N_D obtained by the mWH method. Meanwhile, the spectral lattice thermal conductivity, κ_s, is employed to quantify the contribution of the different scattering mechanisms to the lowered lattice thermal conductivity, as demonstrated in Figure 3e. The results suggest that the grain boundaries are primarily responsible for scattering low-frequency phonons, while the transport of high-frequency phonons is influenced substantially by point defects. By contrast, the contribution of the dislocations covers a broad frequency range, particularly scattering mid- to high-frequency phonons. These results unambiguously reveal that the ultrahigh-pressure process introduces dense dislocations with a N_D of $\approx 9.1 \times 10^{16}$ m^{-2} in $Bi_{0.96}Pb_{0.04}CuSeO$ ceramics, which strongly block phonon transport compared to other scattering mechanisms and are the primary contribution of reducing the κ_l. In addition, the κ_l of $Bi_{0.96}Pb_{0.04}CuSeO$ ceramics prepared under 2 GPa is the lowest over the temperature range of 350–850 K compared to that of superior BiCuSeO-based ceramics with various compositions prepared under much lower pressure (typically ≈50 MPa)(Figure 3f).[18–21,24,47,50] Notably, we found that Ren et al.[20] previously reported a minimum lattice thermal conductivity of 0.13 Wm^{-1} K^{-1} at 873 K in BiCuSeO, which is exactly equal to our lowest lattice thermal conductivity, but the corresponding temperature is higher than ours (767 K). This implies that 0.13 Wm^{-1} K^{-1} could be reached in BiCuSeO-based ceramics, and there is a space for optimization in the lattice thermal conductivity compared to the κ_{diff} of ≈0.07 $Wm^{-1}K^{-1}$.[22]

2.3. Microstructure and Dense Dislocations Formed via Ultrahigh Pressure

To reveal the microstructures and dislocations associated with external pressure, high-magnification transmission electron microscopy (TEM) observations were performed on the $Bi_{0.96}Pb_{0.04}CuSeO$ ceramics prepared under 2 GPa. **Figure 4a** shows abundant grains with a size of ≈10 nm on average, thus forming a high density of grain boundaries. Such architectural features are attributed to the ultrahigh pressure against the contribution of sintering temperature which normally facilitates grain growth. This phenomenon is also consistent with our previous observation.[51,52] To obtain a better statistic, we have performed more TEM observations from random areas of the sample, as shown in Figure S7 (Supporting Information), indicating that the majority of grains have a size of ≈10 nm. A closer examination of the grain boundary area (shadow in Figure 4a) in Figure 4b reveals more atomic structure details. The fast Fourier transform (FFT) patterns for the right and left sides of the grain boundary can be identified as the BiCuSeO structure in the space group of P4/nmm viewed along the [001] and [111] orientations, respectively. Corresponding atomic models viewed along these directions are illustrated in Figure 4c1-2. Further inverse FFT (IFFT) analysis for Figure 4b evidences a large number of geometrically necessary dislocations at the grain boundary (Figure S8, Supporting Information), leading to strong strain fields along both strain components ε_{xx} and ε_{xy}. Besides, an edge dislocation is identified within one grain and a Burgers vector of $\boldsymbol{b} = a/2[111]$ can be determined by drawing the Burgers loop, as depicted in Figure 4d. Actually, more edge dislocations in this area can be revealed by a corresponding IFFT analysis (Figure 4e). These dense dislocations give rise to strong strain fluctuations around the dislocation cores, consequently interlinking and forming the strain domains, as demonstrated by the geometrical phase analysis (GPA) in Figure 4f1-2. Notably, although dense dislocations exist in $Bi_{0.96}Pb_{0.04}CuSeO$ ceramics prepared under 2 GPa, the energy dispersive spectroscopy (EDS) mapping (Figure 4g) manifests that all the elements are distributed homogeneously in the medium-magnification area and follow the nominal composition (Table S4, Supporting Information).

Figure 5a illustrates the 3D distribution of constituting elements of sample $Bi_{0.96}Pb_{0.04}CuSeO$ sintered under 2 GPa measured by atom probe tomography (APT). Elements such as Bi, Cu, Se, and O are homogeneously distributed in the probed volume of ≈50 × 50 × 300 nm^3. In contrast, we observed two planar features, which are enriched in Pb, as can be depicted by the iso-composition surfaces of 2 at.% Pb (Figure 5b). These two planes are identified as Pb-rich grain boundaries (GBs), which are also in line with the small grain sizes revealed by TEM in Figure 4. Note that APT is not a tool that can be used to measure the average grain size with reliable statistics due to its very small field of view. A close-up of the upper GB plane is illustrated in Figure 5c, where many dispersive Pb-rich regions were observed. This is different from the impurity segregation to high-angle GBs as observed in Ag-doped PbTe, where dopants can cover the full plane.[53] It appears that these Pb atoms have segregated to the dislocation cores at GBs, consistent with the TEM observations. Figure 5d presents the composition profile across the upper GB along the yellow arrow. The content of Pb in the matrix is determined to be ≈1 at.%, which is very close to the nominal composition in $Bi_{0.96}Pb_{0.04}CuSeO$. This also implies the high solubility of Pb in BiCuSeO. The content of Pb at the GB is ≈2 at.% with a partition coefficient of 2. We also noticed a significant depletion of oxygen in Figure 5d. This is a typical artifact of APT in determining the composition of oxygen.[54] Oxygen-containing

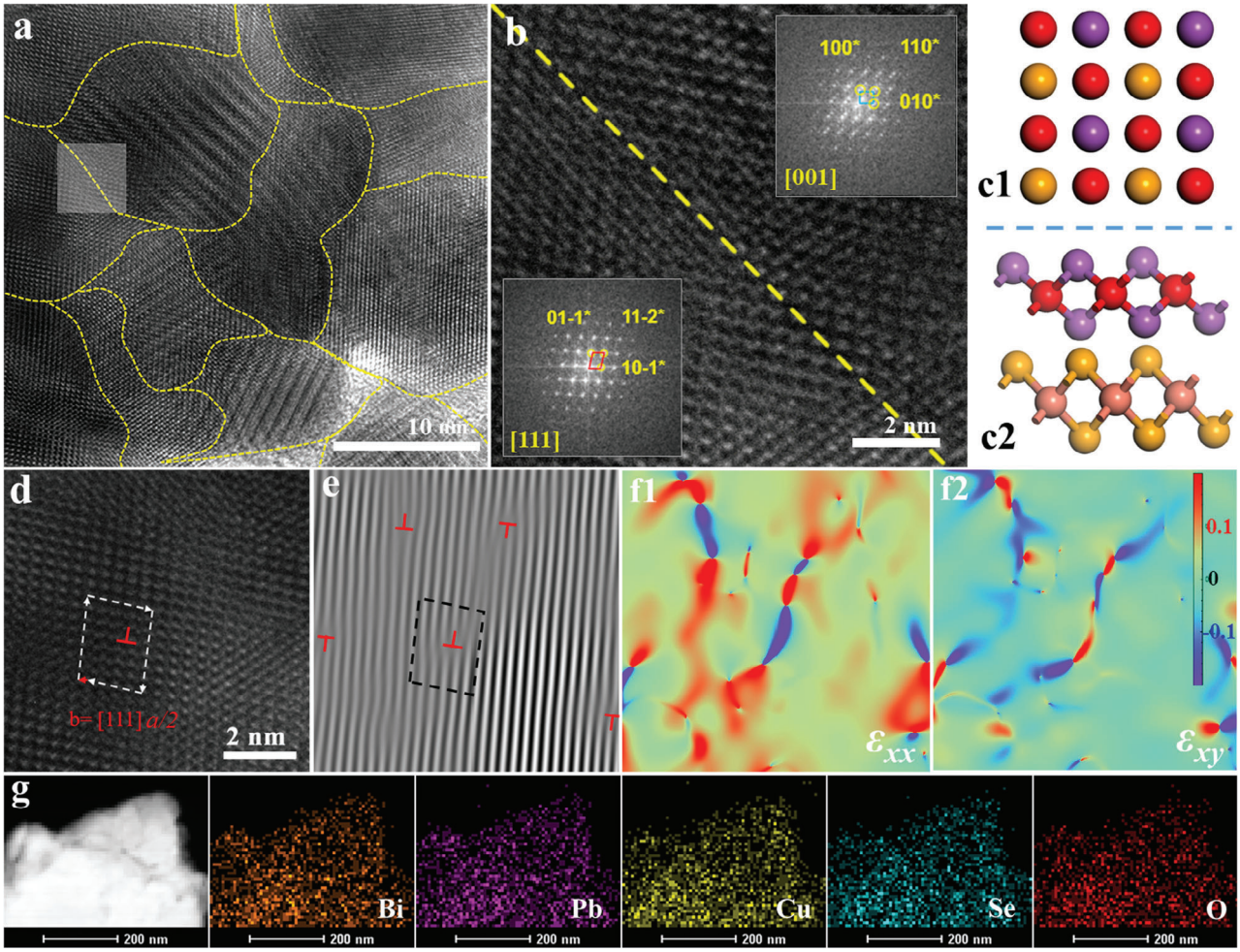

Figure 4. Microstructure and dislocation enabled by ultrahigh pressure. a) HRTEM image including high-density grain boundaries. b) High-magnification TEM image of grain boundary area corresponding to the shadow in a. c) Atomic models of [00l] and [111] orientations. d) Atomic-resolution HRTEM image shows a Burgers circuit and dislocation cores. e) IFFT image taken from d. f) The GPA strain mapping of d in ε_{xx} and ε_{xy}. g) Low-magnification HAADF-STEM image with EDS mapping of Bi, Pb, Cu, Se, and O.

materials can form neutral oxygen during the field evaporation process.[55] These neutral atoms or molecules cannot be detected by the APT detector. Thus, many oxides show a deficiency of oxygen contents in APT measurements. We have proven that the composition in the grain interior is close to the nominal one by EDS (Figure 4g; Table S4, Supporting Information). The segregation of Pb to GBs, or to be more specific, to dislocation cores results from the elastic and electrostatic effect to compensate for the strain and charge around dislocations and GBs.[7,56] These Pb-rich features can form Cottrel atmospheres to pin dislocations and enhance phonon scattering strength at dislocations, as theoretically analyzed by Klemens[57] and experimentally proved by recent studies.[58]

2.4. Mechanism for Dense Dislocations Formation Enabled by Ultrahigh Pressure

To understand the formation of extremely high-density dislocations in $Bi_{0.96}Pb_{0.04}CuSeO$ ceramics during the UHP sintering process, we start by examining the early-stage sintering, where the particles in the mold were further compressed under high pressure and high temperature (HPHT) (**Figure** 6a1-2). According to the modified Ashby's deformation mechanisms map (Figure 6b), at low-shear stress and low-temperature regimes, elastic deformation dominates. As the shear stress and temperature increase, diffusional creep as well as dislocation creep can occur. However, creep is not of main concern under the current high-pressure high-temperature sintering process, where the time scale is much shorter than the conventional creep process. This leads to the activated plastic deformation mechanisms predominantly occurring at much higher stress and temperature,[59] as indicated in the upper right regime in Figure 6b. This is in line with our HPHT experimental approach. The study of the dislocation mechanism on ceramic oxides in recent years[16,60] suggests that homogeneous dislocation nucleation requires extremely high shear stress up to several and tens of GPa depending on the materials and loading conditions, while dislocation multiplication and dislocation motion are active at much lower stress in most ceramics.

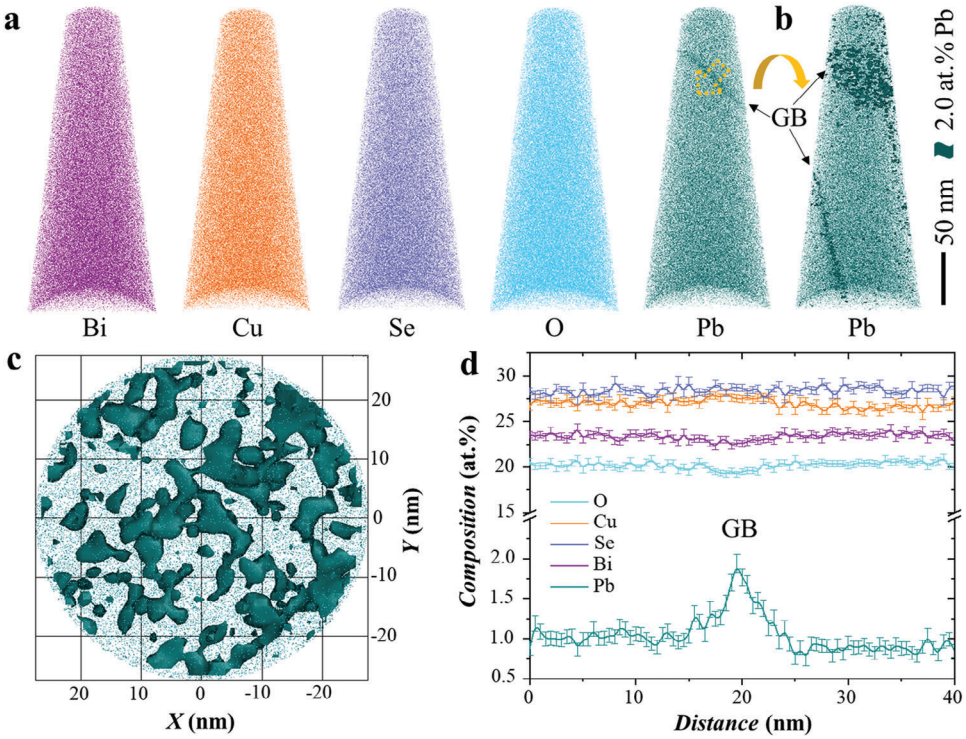

Figure 5. APT characterizations of sample $Bi_{0.96}Pb_{0.04}CuSeO$ prepared under 2 GPa. a) 3D distribution of constituting elements depicted by different color points. b) Pb segregation to the GBs is highlighted by the iso-composition surfaces of 2 at.% Pb and indicated by arrows. c) Top-view of the GB plane, where Pb-rich networks can be observed within the GB plane. d) Composition profile across the upper GB along the yellow arrow, determining the accurate content of Pb in the grain and at the GB.

As the starting ceramic powders normally have few dislocations, dislocation nucleation must be activated during the early-stage sintering. To better illustrate this, a simplified model for two particles in contact has been shown in Figure 6a3. Considering that the initial particle size is small (≈40 nm in the current work) (Figure S9, Supporting Information), the maximum shear stress (located inside the particles underneath the contact neck) induced during the two-particle compression in the normal direction can easily reach the theoretical shear strength ($\approx G/2\pi$, G is the shear modulus) to nucleate dislocations even homogeneously (detailed calculation in Supporting Information; see Figure 6b for dislocation nucleation regime). The fact is that the surface of

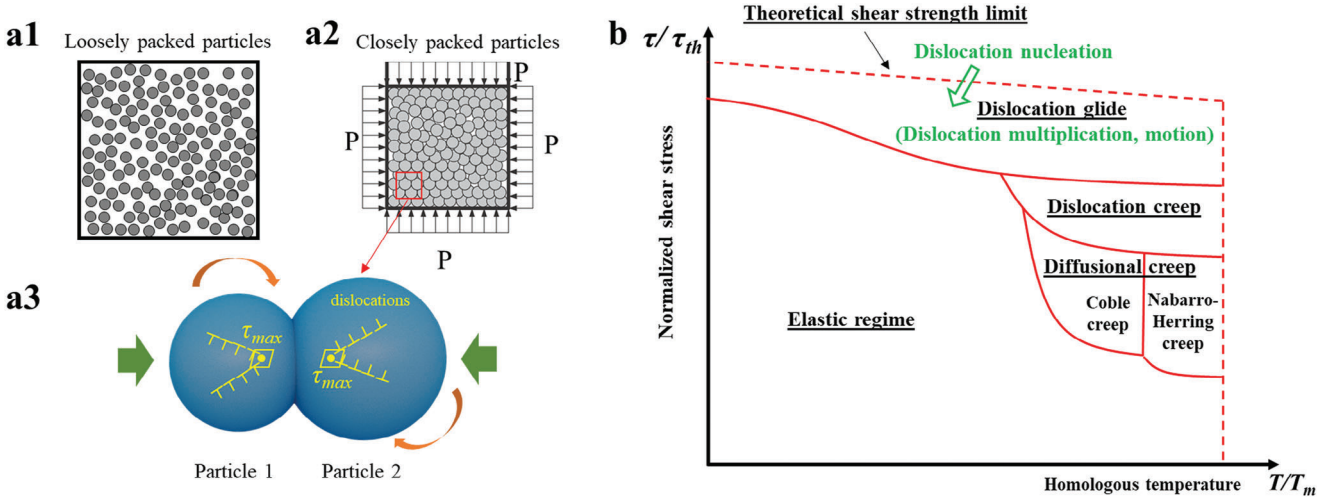

Figure 6. Mechanism of dislocation formation enabled by ultrahigh-pressure. a1-3) Schematic illustration of the high-density dislocations generated during the UHP process. b) Deformation mechanism map with additional dislocation mechanisms (dislocation nucleation, dislocation multiplication, and motion in green color) highlighted.

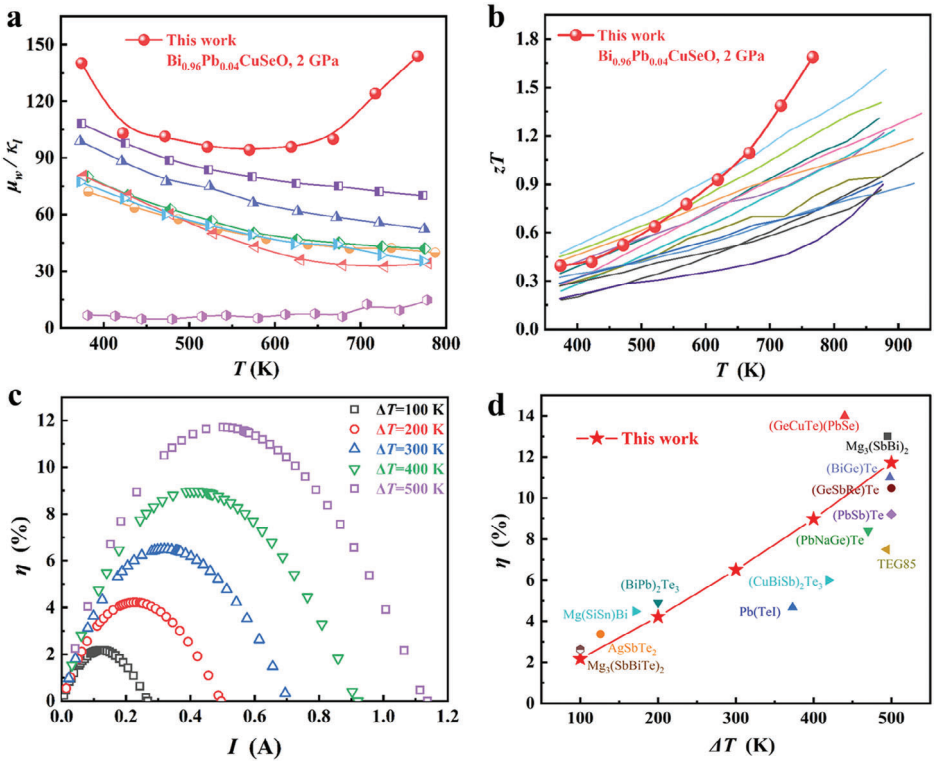

Figure 7. Thermoelectric performance and conversion efficiency. Temperature-dependent a) μ_w/κ_l[21,24,25,27,30,33,63] and b) zT[19–21,24–33] for $Bi_{0.96}Pb_{0.04}CuSeO$ prepared under 2 GPa compared to other high-performance BiCuSeO-based ceramics taken from reported literature. c) Simulated conversion efficiency η as a function of electric current I at temperature difference ΔT of 100–500 K. d) The maximum η at ΔT of 100–500 K for simulated single-leg TE module compared with that of advanced single-leg TE modules with different materials taken from previously theoretical and experimental work.[9,64–74]

the particles is not perfect instead with surface roughness and terraces, which are favorable sites for dislocation nucleation,[61] further reducing the stress level required for dislocation nucleation. Once the nucleation barrier is overcome, dislocation glide as in the deformation mechanism map can be more readily activated, accompanied by extensive dislocation multiplication.[17] However, given that the grain boundaries are abundant in the bulk sample sintered, dislocation motion can be strongly impeded due to the limited slip systems in ceramics.[1] It is therefore expected that some dislocations will pile up at the grain boundaries, as experimentally confirmed by the HRTEM and APT analysis (Figure 5; Figure S8, Supporting Information). Apart from the dominating plastic deformation mediated by dislocations, the grain boundary sliding,[59] grain rotation (Figure 6a3, facilitated by GB dislocations as well as dislocations in the grains[62]), and dislocation creep (dislocation climb and annihilation) can also contribute to the plastic deformation and densification.

2.5. zT Value and Energy Conversion Efficiency in $Bi_{0.96}Pb_{0.04}CuSeO$ Ceramics

With the ultrahigh dense dislocations introduced by the ultrahigh-pressure sintering, the κ_l reduces significantly while the electrical transport properties slightly deteriorate in $Bi_{0.96}Pb_{0.04}CuSeO$ ceramics. To fully evaluate the influence of dense dislocations on electron-phonon transport, the temperature-dependent ratio of weighted mobility to lattice thermal conductivity (μ_w/κ_l) is calculated and compared with high-performance BiCuSeO-based ceramics prepared without applying ultrahigh pressure[21,24,25,27,30,33,63] (**Figure 7a**). The μ_w/κ_l values of $Bi_{0.96}Pb_{0.04}CuSeO$ ceramics prepared under 2 GPa are evidently higher than others over the whole measured temperature, which is primarily ascribed to the ultralow κ_l. This consequently implies the stronger scattering for phonons compared to electrons by dislocations, which is beneficial for the overall thermoelectric properties. Finally, the maximum zT values of $Bi_{0.96}Pb_{0.04}CuSeO$ increase from 0.72 at 767 K for the CA sample to 1.69 for the sample prepared under 2 GPa (Figure S2, Supporting Information). This zT value distinctly outperforms other BiCuSeO and is even record-high in all oxide thermoelectrics[19–21,24–33] (Figure 7b). The corresponding average zT is calculated to be 0.85 at 374–767 K, comparable to the highest zT_{ave} in $Bi_{0.94}Pb_{0.06}Cu_{0.99}Fe_{0.01}SeO$[34] (Figure 1). Additionally, to assess the stability against temperature, the thermal-cycle test is characterized and demonstrates good repeatability and high reliability for $Bi_{0.96}Pb_{0.04}CuSeO$ ceramics prepared under 2 GPa (Figure S10, Supporting Information).

We also estimated the energy conversion efficiency of the best-performing material by an adiabatic system using the COMSOL Multiphysics software (details for the simulation are given in the Experimental Section and Supporting Information). A single-leg

TE module of $Bi_{0.96}Pb_{0.04}CuSeO$ ceramics prepared under 2 GPa was designed to simulate the current-dependent efficiency (η) under different temperature differences (ΔT) (Figure 7c). Benefitting from the high TE performance, a maximum η (T_c = 300 K) as high as ≈12% at ΔT of 500 K is realized (Figure 7c). The η_{max} is higher than all the theoretical and experimental results in single-leg TE modules consisting of various thermoelectric ceramics to the best of our knowledge. By comparison with theory and experiment, it should be mentioned that each η_{max} value at ΔT of 100–500 K obtained in this work is comparable to that of advanced single-leg TE modules made by classic thermoelectric materials such as Bi_2Te_3, PbTe, and GeTe[9,64–74] (Figure 7d). These merits demonstrate great application prospects in the mid-temperature range for $Bi_{0.96}Pb_{0.04}CuSeO$ ceramics prepared by the ultrahigh-pressure process. It is worth noting that the practical conversion efficiency of a TE device is smaller than the theoretical maximum mainly due to the interfacial electrical resistance. Especially for oxides, the contact resistance between electrodes and the material could be very high due to the mismatch in work function and microstructures. The recently developed concepts such as phase diagram high throughput calculations[75] could offer some insights into the design of better thermoelectric interfacial materials for oxides.

3. Conclusion

In summary, we achieved extremely high dislocation density through a unique approach, i.e., ultrahigh-pressure sintering. The dislocation density can reach ≈9.1×10^{16} m^{-2} in $Bi_{0.96}Pb_{0.04}CuSeO$ ceramics prepared under 2 GPa. Meanwhile, the mechanism of dense dislocation formation enabled by ultrahigh pressure is clarified for a better understanding of dislocations caused by ultrahigh pressure in ceramic materials. Owing to the dense dislocations, the phonon transport is strongly suppressed, significantly reducing the lattice thermal conductivity to 0.13 Wm^{-1} K^{-1} and motivating an enhancement in the thermoelectric performance, resulting in a maximum zT of 1.69 at 767 K in $Bi_{0.96}Pb_{0.04}CuSeO$ ceramics prepared under 2 GPa, a record-breaking figure of merit in ceramic oxides. The improved performance renders a maximum η simulated for a single-leg thermoelectric module that achieves ≈12% at ΔT of 500 K. This work demonstrates that ultrahigh-pressure sintering is an effective approach in physics for introducing high-density dislocations, it can overcome the difficulty of dislocation manipulation in ceramics and provides a novel strategy to tailor the functional properties of ceramic oxides.

4. Experimental Section

Synthesis—Sample Powders: High-purity powders of Bi (5N, Aladdin Ltd.), Cu (4N, Sinopharm Ltd.), Se (4N, Aladdin Ltd.), Pb (5N, Sinopharm Ltd.), and Bi_2O_3 (5N, Sinopharm Ltd.) were weighed and mixed according to the stoichiometric composition of $Bi_{1-x}Pb_xCuSeO$ (x = 0, 0.02, 0.04, 0.06, and 0.08). The mixtures were sintered at a rate of 2 °C min^{-1} under an Ar (99.99%) atmosphere using a tubular furnace (MTI 1200X). The raw materials were heated up to 350 °C for 3 h, then increased to 800 °C for 8 h, and finally furnace cooled to room temperature. The sintered products were ground and divided into several groups for preparing samples at various conditions. The control sample was prepared in a vacuum by a conventional approach (CA) using hot-press sintering at 50 MPa and 510 °C for 30 min. Other groups of powders were prepared under ultrahigh-pressure (UHP) of 1–3.5 GPa and 510 °C for 30 min, where such high pressure can exhaust air around the sample and was similar to a vacuum. At the beginning of the UHP process, the pressure increased rapidly to the target pressure value and then was held stably, where the pressure was isostatic and came from six directions of a cubic sample chamber (Figure S11, Supporting Information).

Synthesis—Ultrahigh-Pressure Process: The sample powders were collected and then cold-pressed simply to form a pellet of φ 10.5 × 12 mm. The pellet was assembled into a specific chamber (Figure S11, Supporting Information) in order to be installed in a large-volume cubic anvil ultrahigh-pressure apparatus (SPD 6×1200), as depicted in Figure S12 (Supporting Information). To employ the ultrahigh-pressure apparatus, the pressure and temperature were loaded to the sample forming a high-pressure and high-temperature (HPHT) condition with a rate of 7.5 MPa s^{-1} and 3 °C s^{-1}. The heating temperature was held at 510 °C under different ultrahigh pressures of 1–3.5 GPa for 30 min, then quenched and unloaded pressure rapidly. To ensure the accuracy of the experimental conditions, the loaded pressure was calibrated by the change in resistance of standard substances, and the temperature was measured by a Pt30 Rh/Pt6 Rh thermocouple junction placed near the sample.

Structural Characterization: Phase structure was identified by X-ray diffraction (SmartLab SE D/teX Ultra250 diffractometer, Rigaku, Japan) with Cu Kα (λ = 1.5418 Å) radiation in a reflection geometry on a diffractometer operating at 3 kW. The XRD data was refined by the Rietveld method, which was operated using the GSAS software package. The transmission electron microscopy equipped with energy dispersive X-ray spectroscopy (EDS; JEOL JEM-2200FS, Japan) was used to observe the microstructure by collecting HRTEM images and to determine the spatially resolved elemental compositions. Needle-shaped APT specimens were prepared by the site-specific "lift-out" method, using a dual-beam scanning electron microscope/focused ion beam (Helios NanoLab 650, FEI). The specimens were measured in a local electrode atom probe (LEAP 5000 XS, Cameca) by applying 10 ps, 7.5 pJ UV (wavelength = 355 nm) laser pulses with a pulse repetition rate of 200 kHz. The detection rate was 5 ions per 1000 pulses on average (0.5%) and the ion flight path was 100 mm. The base temperature of the specimen was set at 40 K to minimize the atom diffusions. The detection efficiency of this microscope was limited to 80% owing to the open area left between the microchannels on the detector plates. The APT data were processed using the commercial software package AP Suite 6.3.

Transport Properties Measurements: The final products were cut and polished into bars with dimensions of 2.5 × 2.5 × 9 mm^3 and disks of φ 10 mm × 1.5 mm. The bars were measured from 374 to 767 K in a helium atmosphere using thermoelectric equipment (Namicro-3LT, JouleYacht, China) to obtain the Seebeck coefficient and electrical conductivity. The disks were used for the measurement of thermal diffusivity, λ, via a laser flash instrument (Netzsch LFA467, Germany). The specific heat, C_p, was estimated by the Dulong–Petit limit, $C_p = 3nR$, where n is the number of atoms per formula unit and R is the gas constant. The sample density, D, was determined by the Archimedes' method. Thus, the total thermal conductivity, κ, was calculated via the equation, $\kappa = DC_p\lambda$. The electronic thermal conductivity, κ_e, was calculated using the Wiedemann–Franz law $\kappa_e = \sigma LT$, where the Lorenz number, L, was estimated by the single parabolic band model. The lattice thermal conductivity, κ_l, was determined by subtracting κ_e from κ. These shaped samples for all the measurements were cut from the same specimen and orientation.

Stimulation of Single-Leg Thermoelectric Modules: To evaluate the application potential of superior samples prepared in the work, the 3D finite-element simulations of a single-leg thermoelectric (TE) module were performed by the COMSOL Multiphysics software. A geometrical TE module was designed in the software interface, as displayed in Figure S14 (Supporting Information), which was assembled with Al_2O_3 substrates, Ag electrodes, and a superior sample leg. Al_2O_3 substrates with the dimensions ($l_x \times l_y \times l_z$) of 4.5 × 3 × 1 mm^3 were used for electrical insulation and immobilization, and Ag electrodes with a thickness of 0.06 mm were used to make a connection between the samples and Al_2O_3 substrates. The height (H) and cross-sectional area (A) of the superior sample leg were

15 mm and 4.5 × 3 mm^2, respectively, which were adopted from previously reported single-leg TE modules with oxide thermoelectric materials.[76] The physical properties of Al_2O_3 and Ag are given in Table S6 (Supporting Information). Herein, the electrical and thermal contact resistances between these interfaces were not considered in the simulation model. The measured temperature-dependent TE properties of $Bi_{0.96}Pb_{0.04}CuSeO$ prepared under 2 GPa were used for simulation, and more detailed simulation processes can be found in Supporting Information.

Supporting Information

Supporting Information is available from the Wiley Online Library or from the author.

Acknowledgements

This work was supported by the Natural Science Foundation of Jilin Province, China (Grant No. 20200201254JC), the Education Department of Jilin Province, China (Grant No. JJKH20220761KJ), and the Program of Youth Talents of Jilin Association of Science and Technology (Grant No. 181906). X. Fang acknowledges the financial support from the European Union (ERC, Project MECERDIS, Grant No. 101076167).

Conflict of Interest

The authors declare no conflict of interest.

Author Contributions

Z.Y. and H.Z. contributed equally to this work. X.G., Y.Y., and X.F. designed and supervised the work. X.G., Y.Y., and X.F. analyzed the data as well as reviewed and edited the draft. Y.Y. accomplished the APT characterizations and analysis. X.F. discussed dislocation deformation mechanisms. X.G. and X.W. performed theoretical simulations and analysis for a single-leg thermoelectric module. Z.X.Y., H.Z., and Y.Q.W. prepared samples and characterized the thermoelectric properties and the microstructure. Z.X.Y. and H.Z. processed the data visualization and wrote the original draft. Y.Q.W., Y.W., and Y.B.X. carried out the data validation and curation. All authors have approved the results and conclusions of this work.

Data Availability Statement

The data that support the findings of this study are available from the corresponding author upon reasonable request.

Keywords

dislocation, BiCuSeO, Ceramic, Thermoelectric, ultrahigh pressure sintering

Received: July 20, 2024
Revised: September 26, 2024
Published online:

[1] J. P. Hirth, J. Lothe, T. Mura, *J. Appl. Mech.* **1983**, *50*, 476.
[2] L. E. Levine, B. C. Larson, W. Yang, M. E. Kassner, J. Z. Tischler, M. A. Delos-Reyes, R. J. Fields, W. Liu, *Nat. Mater.* **2006**, *5*, 619.
[3] M. Li, Y. Shen, K. Luo, Q. An, P. Gao, P. Xiao, Y. Zou, *Nat. Mater.* **2023**, *22*, 958.
[4] X. Fang, J. Rödel, *Nat. Mater.* **2023**, *22*, 943.
[5] M. Al Malki, Y. Liu, J. Male, V. P. Dravid, D. C. Dunand, G. J. Snyder, *Acta Mater.* **2024**, *266*, 119652.
[6] M. N. Gurusinghe, T. G. Andersson, *Phys. Rev. B* **2003**, *67*, 235208.
[7] Y. Yu, A. Sheskin, Z. Y. Wang, A. Uzhansky, Y. Natanzon, M. Dawod, L. Abdellaoui, T. Schwarz, C. Scheu, M. Wuttig, *Adv. Energy Mater.* **2024**, *14*, 2304442.
[8] L. Xu, Y. Xiao, S. Wang, B. Cui, D. Wu, X. Ding, L.-D. Zhao, *Nat. Commun.* **2022**, *13*, 6449.
[9] Y. Jiang, J. Dong, H. Zhuang, J. Yu, B. Su, H. Li, J. Pei, F. Sun, M. Zhou, H. Hu, J. Li, Z. Han, B. Zhang, T. Mori, J. Li, *Nat. Commun.* **2022**, *13*, 6087.
[10] Y. Wu, Z. Chen, P. Nan, F. Xiong, S. Lin, X. Zhang, Y. Chen, L. Chen, B. Ge, Y. Pei, *Joule* **2019**, *3*, 1276.
[11] S. I. Kim, K. H. Lee, H. A. Mun, H. S. Kim, S. W. Hwang, J. W. Roh, D. J. Yang, W. H. Shin, X. Li, Y. H. Lee, *Science* **2015**, *348*, 109.
[12] Z. Chen, B. Ge, W. Li, S. Lin, J. Shen, Y. Chang, R. Hanus, G. J. Snyder, Y. Pei, *Nat. Commun.* **2017**, *8*, 13828.
[13] Z. Chen, Z. Jian, W. Li, Y. Chang, B. Ge, R. Hanus, J. Yang, Y. Chen, M. Huang, G. J. Snyder, *Adv. Mater.* **2017**, *29*, 1606768.
[14] F. Guo, B. Cui, Y. Liu, X. Meng, J. Cao, Y. Zhang, R. He, W. Liu, H. Wu, S. J. Pennycook, *Small* **2018**, *14*, 1802615.
[15] Y. Yu, M. Cagnoni, O. Cojocaru-Mirédin, M. Wuttig, *Adv. Funct. Mater.* **2020**, *30*, 1904862.
[16] X. Fang, *J. Am. Ceram. Soc.* **2024**, *107*, 1425.
[17] X. Fang, H. Bishara, K. Ding, H. Tsybenko, L. Porz, M. Höfling, E. Bruder, Y. Li, G. Dehm, K. Durst, *J. Am. Ceram. Soc.* **2021**, *104*, 4728.
[18] J. Lan, Y. Liu, B. Zhan, Y. Lin, B. Zhang, X. Yuan, W. Zhang, W. Xu, C. Nan, *Adv. Mater.* **2013**, *25*, 5086.
[19] J. Li, J. Sui, Y. Pei, C. Barreteau, D. Berardan, N. Dragoe, W. Cai, J. He, L.-D. Zhao, *Energy Environ. Sci.* **2012**, *5*, 8543.
[20] G. Ren, S. Wang, Z. Zhou, X. Li, J. Yang, W. Zhang, Y. Lin, J. Yang, C. Nan, *Nat. Commun.* **2019**, *10*, 2814.
[21] Y. Gu, X. Shi, L. Pan, W. Liu, Q. Sun, X. Tang, L. Kou, Q. Liu, Y. Wang, Z. Chen, *Adv. Funct. Mater.* **2021**, *31*, 2101289.
[22] M. T. Agne, R. Hanus, G. J. Snyder, *Energy Environ. Sci.* **2018**, *11*, 609.
[23] Y. Liu, L.-D. Zhao, Y. Zhu, Y. Liu, F. Li, M. Yu, D. Liu, W. Xu, Y. Lin, C. Nan, *Adv. Energy Mater.* **2016**, *6*, 1502423.
[24] G. Ren, S. Wang, Y. Zhu, K. J. Ventura, X. Tan, W. Xu, Y. Lin, J. Yang, C. Nan, *Energy Environ. Sci.* **2017**, *10*, 1590.
[25] Y. Gu, W. Ai, L. Pan, X. Hu, P. Zong, C. Chen, C. Lu, Z. Xu, Y. Wang, *Mater. Today Phys.* **2022**, *24*, 100688.
[26] Y. Pei, H. Wu, D. Wu, F. Zheng, J. He, *J. Am. Chem. Soc.* **2014**, *136*, 13902.
[27] J. Tang, R. Xu, J. Zhang, D. Li, W. Zhou, X. Li, Z. Wang, F. Xu, G. Tang, G. Chen, *ACS Appl. Mater. Interfaces* **2019**, *11*, 15543.
[28] F. Li, Z. Zheng, Y. Chang, M. Ruan, Z. Ge, Y. Chen, P. Fan, *ACS Appl. Mater. Interfaces* **2019**, *11*, 45737.
[29] J. Sui, J. Li, J. He, Y. Pei, D. Berardan, H. Wu, N. Dragoe, W. Cai, L.-D. Zhao, *Energy Environ. Sci.* **2013**, *6*, 2916.
[30] J. Li, J. Sui, Y. Pei, X. Meng, D. Berardan, N. Dragoe, W. Cai, L.-D. Zhao, *J. Mater. Chem. A* **2014**, *2*, 4903.
[31] F. Li, M. Ruan, Y. Chen, W. Wang, J. Luo, Z. Zheng, P. Fan, *Inorg. Chem. Front.* **2019**, *6*, 799.
[32] D. Yang, X. Su, Y. Yan, T. Hu, H. Xie, J. He, C. Uher, M. G. Kanatzidis, X. Tang, *Chem. Mater.* **2016**, *28*, 4628.
[33] G. Ren, S. Butt, K. J. Ventura, Y. Lin, C. Nan, *RSC Adv.* **2015**, *5*, 69878.
[34] L. Pan, Y. Lang, L. Zhao, D. Berardan, E. Amzallag, C. Xu, Y. Gu, C. Chen, L.-D. Zhao, X. Shen, *J. Mater. Chem. A* **2018**, *6*, 13340.
[35] H. Zhu, Z. Li, C. Zhao, X. Li, J. Yang, C. Xiao, Y. Xie, *Natl. Sci. Rev.* **2021**, *8*, nwaa085.

[36] F. Li, J. Li, L.-D. Zhao, K. Xiang, Y. Liu, B. Zhang, Y. Lin, C. Nan, H. Zhu, *Energy Environ. Sci.* **2012**, *5*, 7188.
[37] Z. Yin, Z. Liu, Y. Yu, C. Zhang, P. Chen, J. Zhao, P. He, X. Guo, *ACS Appl. Mater. Interfaces* **2021**, *13*, 57638.
[38] L.-D. Zhao, J. He, D. Berardan, Y. Lin, J. Li, C. Nan, N. Dragoe, *Energy Environ. Sci.* **2014**, *7*, 2900.
[39] T. Lyu, Q. Yang, Z. Li, C. Zhang, F. Liu, J. Li, L. Hu, G. Xu, *ACS Appl. Mater. Interfaces* **2023**, *15*, 19250.
[40] Q. Chen, L. Chang, X. Li, Y. Wang, J. Wang, Y. Zhang, H. Ma, X. Jia, *Ceram. Int.* **2021**, *47*, 20910.
[41] B. Cai, J. Li, H. Sun, L. Zhang, B. Xu, W. Hu, D. Yu, J. He, Z. Zhao, Z. Liu, *Sci. China Mater* **2018**, *61*, 1218.
[42] Q. Zhang, C. Chen, N. Li, Q. Huang, Y. He, X. Liu, B. Wang, D. Zhang, D. Y. Kim, Y. Wang, *J. Phys. Chem. C* **2018**, *122*, 15929.
[43] D. Zou, Y. Liu, S. Xie, J. Lin, H. Zheng, J. Li, *RSC Adv.* **2014**, *4*, 54819.
[44] Z. Liu, X. Guo, R. Li, J. Qin, H. Li, X. Chen, X. Zhou, *J. Materiomics* **2019**, *5*, 649.
[45] T. Ungár, A. Borbély, *Appl. Phys. Lett.* **1996**, *69*, 3173.
[46] T. Ungár, S. Ott, P. G. Sanders, A. Borbély, J. R. Weertman, *Acta Mater.* **1998**, *46*, 3693.
[47] R. Xu, Z. Chen, Q. Li, X. Yang, H. Wan, M. Kong, W. Bai, N. Zhu, R. Wang, J. Song, *Research* **2023**, *6*, 0123.
[48] J. Callaway, H. C. von Baeyer, *Phys. Rev.* **1960**, *120*, 1149.
[49] Y. Sun, Y. Zhou, J. Han, W. Liu, C. Nan, Y. Lin, M. Hu, B. Xu, *Npj Comput. Mater.* **2019**, *5*, 97.
[50] Y. Liu, L.-D. Zhao, Y. Liu, J. Lan, W. Xu, F. Li, B. Zhang, D. Berardan, N. Dragoe, Y. Lin, *J. Am. Chem. Soc.* **2011**, *133*, 20112.
[51] Z. Liu, X. Guo, M. Yu, D. Wang, J. Qin, F. Jin, X. Xue, *J. Alloys Compd.* **2020**, *812*, 152106.
[52] H. Zhang, C. Zhang, D. H. Gregory, Z. Yin, Y. Wang, P. He, X. Guo, *J. Phys. D: Appl. Phys.* **2023**, *56*, 183001.
[53] R. Wu, Y. Yu, S. Jia, C. Zhou, O. Cojocaru-Mirédin, M. Wuttig, *Nat. Commun.* **2023**, *14*, 719.
[54] S. H. Kim, S. Bhatt, D. K. Schreiber, J. Neugebauer, C. Freysoldt, B. Gault, S. Katnagallu, *New J. Phys.* **2024**, *26*, 033021.
[55] B. Gault, D. W. Saxey, M. W. Ashton, S. B. Sinnott, A. N. Chiaramonti, M. P. Moody, D. K. Schreiber, *New J. Phys.* **2016**, *18*, 033031.
[56] Z. Huang, F. Wang, C. Jung, S. Zhang, F. Zu, C. Zhou, Y. Yu, *Mater. Today Phys.* **2023**, *37*, 101198.
[57] P. G. Klemens, *J. Appl. Phys.* **1968**, *39*, 5304.
[58] L. Abdellaoui, Z. Chen, Y. Yu, T. Luo, R. Hanus, T. Schwarz, R. Bueno Villoro, O. Cojocaru-Mirédin, G. J. Snyder, D. Raabe, *Adv. Funct. Mater.* **2021**, *31*, 2101214.
[59] H. Xu, W. Ji, W. Guo, Y. Li, J. Zou, W. Wang, Z. Fu, *Adv. Sci.* **2022**, *9*, 2104532.
[60] X. Fang, A. Nakamura, J. Rödel, *Am. Ceram. Soc. Bull.* **2023**, *102*, 24.
[61] J. A. Zimmerman, C. L. Kelchner, P. A. Klein, J. C. Hamilton, S. M. Foiles, *Phys. Rev. Lett.* **2001**, *87*, 165507.
[62] Q. Liu, Z. Xiong, X. Liu, L. Fang, C. Lv, J. Yang, Y. Liu, Y. Zhang, W. Zhu, J. Li, *J. Appl. Phys.* **2023**, *134*, 185903.
[63] Y. Liu, Y. Zhu, W. Liu, A. Marcelli, W. Xu, *J. Am. Ceram. Soc.* **2019**, *102*, 1541.
[64] Z. Bu, X. Zhang, B. Shan, J. Tang, H. Liu, Z. Chen, S. Lin, W. Li, Y. Pei, *Sci. Adv.* **2021**, *7*, eabf2738.
[65] Y. Zhang, Z. Li, S. Singh, A. Nozariasbmarz, W. Li, A. Genç, Y. Xia, L. Zheng, S. H. Lee, S. K. Karan, *Adv. Mater.* **2023**, *35*, 2208994.
[66] H. Hu, H. Zhuang, Y. Jiang, J. Shi, J. Li, B. Cai, Z. Han, J. Pei, B. Su, Z. Ge, *Adv. Mater.* **2021**, *33*, 2103633.
[67] A. Suwardi, S. H. Lim, Y. Zheng, X. Wang, S. W. Chien, X. Tan, Q. Zhu, L. M. N. Wong, J. Cao, W. Wang, Q. Yan, C. K. I. Tan, J. Xu, *J. Mater. Chem. C* **2020**, *8*, 16940.
[68] K. Cheng, Z. Bu, J. Tang, X. Zhang, X. Meng, W. Li, Y. Pei, *Mater. Today Phys.* **2022**, *28*, 100887.
[69] Z. Liang, L. Deng, X. Shi, S. Song, C. Xu, C.-W. Chu, Z. Ren, *Mater. Today Energy* **2022**, *29*, 101099.
[70] X. Wu, Y. Lin, Z. Han, H. Li, C. Liu, Y. Wang, P. Zhang, K. Zhu, F. Jiang, J. Huang, *Adv. Energy Mater.* **2022**, *12*, 2203039.
[71] T. Parashchuk, I. Horichok, A. Kosonowski, O. Cherniushok, P. Wyzga, G. Cempura, A. Kruk, K. T. Wojciechowski, *J. Alloys Compd.* **2021**, *860*, 158355.
[72] P. Sauerschnig, P. Jood, M. Ohta, *Adv. Mater. Technol.* **2023**, *8*, 2201295.
[73] S. Chen, Y. Wang, Y. Wang, W. Fan, J. Guo, J. Chen, Y. Jiang, R. A. A. Al-Yusufi, Z. A. Munir, *J. Alloys Compd.* **2022**, *905*, 164267.
[74] A. K. Bohra, R. Bhatt, A. Singh, S. Bhattacharya, R. Basu, K. N. Meshram, S. K. Sarkar, P. Bhatt, P. K. Patro, D. K. Aswal, *Mater Design* **2018**, *159*, 127.
[75] L. Xie, L. Yin, Y. Yu, G. Peng, S. Song, P. Ying, S. Cai, Y. Sun, W. Shi, H. Wu, *Science* **2023**, *382*, 921.
[76] T. Chen, J. Wang, X. Wang, H. Wang, W. Su, J. Zhai, F. Mehmood, M. Khan, C. Wang, *Appl. Mater. Today* **2022**, *29*, 101557.